SCIENCEDOMAIN

In vitro Evaluations of Anodic Spark Deposited AZ91 Alloy as Biodegradable Metallic Orthopedic Implant

Mehdi Razavi[1,3,4,5*], Mohammadhossein Fathi[1,2], Omid Savabi[3], Daryoosh Vashaee[5] and Lobat Tayebi[4,6*]

[1]*Biomaterials Research Group, Department of Materials Engineering, Isfahan University of Technology, Isfahan 84156-83111, Iran.*
[2]*Dental Materials Research Center, Isfahan University of Medical Sciences, Isfahan, Iran.*
[3]*Torabinejad Dental Research Center, School of Dentistry, Isfahan University of Medical Sciences, Isfahan 81746-73461, Iran.*
[4]*School of Materials Science and Engineering, Helmerich Advanced Technology Research Center, Oklahoma State University, Tulsa, OK 74106, USA.*
[5]*School of Electrical and Computer Engineering, Helmerich Advanced Technology Research Center, Oklahoma State University, Tulsa, OK 74106, USA.*
[6]*School of Chemical Engineering, Oklahoma State University, Stillwater, OK 74078, USA.*

Authors' contributions

This work was carried out in collaboration between all authors. Author MR designed the study, performed the statistical analysis, wrote the protocol, and wrote the first draft of the manuscript. Authors MHF, OS, DV and LT managed the analyses of the study. All authors read and approved the final manuscript.

Original Research Article

ABSTRACT

Surface treatment of Mg alloys is a major approach for its enhanced use as orthopedic implants. In this paper, the *in vitro* bioactivity, mechanical stability and cytocompatibility of the AZ91 Mg alloy coated by anodic spark deposition (ASD) method are studied. The cytocompatibility behavior is examined by culturing L-929 fibroblast on the surface of the uncoated and ASD-coated AZ91 Mg substrates. The results showed that the corrosion resistance, *in vitro* bioactivity, mechanical stability and cytocompatibility of biodegradable Mg alloy were improved by ASD coating. Reduction of the degradation rate by ASD coating

_____

*Corresponding author: Email: lobat.tayebi@okstate.edu, m.razavi@ma.iut.ac.ir;

not only created a relatively stable interface for the cell adhesion and growth, but also arrested the release of corrosion products to reduce the cytotoxicity, hence, resulting in the enhanced cytocompatibility.

1. INTRODUCTION

Metallic and ceramic biomaterials such as stainless steels, cobalt–chromium–based alloys, bioactive glasses and titanium alloys have been widely used for repair of damaged bone tissue in load–bearing applications [1-3]. Although they have good mechanical properties, a re-surgery might be required to remove them after implanting in the body [4]. Using biodegradable metal with good elastic modulus and ultimate strength, such as Mg alloys, can resolve this problem [5]. Mg alloys can degrade slowly in the biological environment, a characteristic that makes them suitable as implants in orthopedic and vascular stents applications [6]. Mg–based implants have a density of 1.74–2.0 g/cm^3 and elastic moduli of 41–45 GPa, which are close to that of bone (20-25 GPa), and thus preventing stress shielding phenomenon [1]. Biodegradable Mg alloy implants can be more suitable for load bearing applications than biodegradable polymeric implants due to their superior mechanical strength [1]. Previous *in vivo* and *in vitro* studies have shown that Mg alloys can exhibit good biocompatibility [7]. In addition, increased minerals and bone mass were found around the Mg implants in bone [5]. The beneficial influence of Mg has been emphasized further in a study showing that the bone–implant interface strength and osseointegration are significantly greater for Mg than for conventional titanium materials [6]. However, the degradation is complemented by production of hydrogen bubbles which is harmful for the body due to the gas accumulations in the surrounding tissue [8]. To prepare the Mg alloys for biomedical applications, aside retarding degradation rate, the bioactivity, mechanical stability and cytocompatibility should also be enhanced [9]. One of the effective approaches to reducing corrosion propensity of metal implant is by surface modification [10,11]. This may also improve the surface bioactivity and cytocompatibility of the material [12,13]. It is possible to reduce the corrosion of Mg alloy, improve its surface bioactivity, mechanical stability and cytocompatibility through appropriate surface treatment selection [1,14,15]. Electrochemical plating, chemical conversion coating, physical vapour deposition, laser surface treatment and anodization are among various methods that have been used to improve the surface properties of Mg alloy for biomedical applications [10]. Among these techniques, anodization is one of the most effective and popular methods [16,17] used to decrease the corrosion rate of Mg alloys. However, the traditional anodization method can only work under relatively low operating voltage and this limits the properties of the coating. A new anodization technology termed anodic spark deposition (ASD), has recently been developed to overcome this problem [18,19]. ASD works with a high–voltage discharge such that a coating can be formed in situ on the surface of the Mg substrate [20]. During ASD discharges, plasma is produced and an oxide layer grows. The process involves melting and rapid solidification of the growing oxide. Such layers have more corrosion resistance compared to the chemical conversion layers [21]. Overall, ASD layers are very stable, hard and resistant to abrasion and corrosion [22]. For orthopaedic implants such layers when used could slow down the corrosion rate and increase the *in vitro* bioactivity [18,21]. Therefore, in this work a comprehensive study on the mechanical stability, biocompatibility, corrosion and bioactivity of ASD-coated biodegradable Mg alloy for orthopedic implants is presented.

2. MATERIALS AND METHODS

2.1 Materials

Plate samples (2×15×5 mm) from an AZ91 Mg alloy ingot with nominal composition of 9 wt.% aluminium and 1 wt.% zinc are prepared. Before the ASD process, the samples are polished with the SiC papers and then cleaned with acetone.

A DC power supply is used while the anode and the cathode are AZ91 samples and stainless steel, respectively. The electrolyte is a solution of 200 g/L sodium silicate and 200 g/L sodium hydroxide. The ASD process is carried out for 30 min at a 60 V potential. Fig. 1 shows a diagram about ASD coating process indicating the coating parameters.
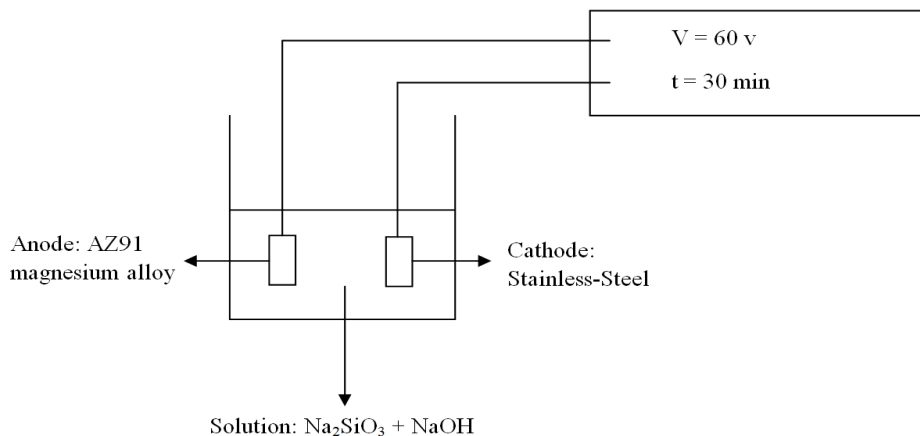

Fig. 1. A diagram about ASD coating process indicating the coating parameters

2.2 Surface Characterization

The phase composition of samples is studied using X–ray diffraction technique (XRD, Philips X'Pert). The surface crystal structure of the samples (before and after the immersion test) is analyzed using a scanning electron microscope (Philips XL 30: Eindhoven) equipped with energy–dispersive spectroscopy (EDS). Laser scanning electron microscope (Keyence, VK X100/X200) is used to observe the topography and roughness of the samples using three dimensional images. The VK analyzer is utilized to study the acquired data from the microscope.

2.3 Corrosion Testing

Electrochemical tests are performed by an Ametek potentiostat (model PARSTAT 2273).The corrosion test electrolyte is a simulated body fluid (SBF) prepared according to Kokoubo's protocol [23]. The electrochemical measurement was conducted using a conventional three-electrodes electrochemical cell containing 70 mL SBF. The uncoated and ASD coated samples, a platinum rod and a saturated calomel electrode, acted as working electrode, auxiliary electrode and reference electrode respectively. Before the experiment, the samples were stabilized in SBF solution for 60 min. The EIS were adjusted in a frequency range of 100 kHz-10 mHz. The sample area used during the corrosion test was 1 cm^2.

The immersion test was performed according to ASTM-G31-72 [24]. The samples are immersed in cylindrical bottles filled with SBF in a water bath at 37ºC for 0, 72, 168, 336, 504 and 672 hrs. For the *in vitro* bioactivity evaluation, typical immersion morphology is characterized by SEM. After this examination, the uncoated and ASD coated samples were immersed in chromic acid (180 g/L) [25] to remove the corrosion products. In order to decrease the reaction between MgO in ASD coating layer and chromic acid, the time of immersing the samples in chromic acid is minimized to 10 min. Moreover, after removing the corrosion products, the samples were washed rapidly. In each experiment, three samples were examined and the mean ± SD was reported.

The amount of Mg ion release was into the SBF, was measured by ICP technique (ICP: PERKIN–ELMER 2380). The pH values of samples are also measured with a pH–Meter (pH & ION meter GLP 22, Crison, Spain). Fourier Transform Infrared spectroscopy (FTIR, Agilent 680 IR) was used to analyze the precipitated products on the surface of samples during the degradation in SBF.

2.4 Mechanical Testing

Compression test was carried out according to ASTM E9 standard [26] by an INSTRON universal tensile testing machine to measure the residual compressive properties for each sample after immersion test.

2.5 Biocompatibility Studies

For the cytocompatibility test, L–929 fibroblast cell line is used. The cells are first cultured in 89% Dulbecco's modified Eagle's medium (DMEM, Gibco) supplemented with 10% fetal bovine serum (FBS, Gibco), and 1% penicillin streptomycin. The L–929 fibroblasts are seeded in T–75 plates at a density of 3000 cells/mL, incubated at 37ºC in humidified 5% CO_2 atmosphere for 5 days and the medium is renewed after 3 days. The samples are sterilized and the cells are seeded onto both uncoated and coated samples. Cell viability and attachment are examined in 6 well plates (Corning, NY, USA) after 2, 5 and 7 days at 37 °C with 5% CO_2 in a humidified incubator, where triplicate samples are examined at each time point. DMEM medium is used for negative control samples. At the end of each incubation time, the mediums are discarded and replaced by MTT solution (3-(4,5-dimethylthiazol)-2,5-diphenyltetrazoliumbromide). MTT solution is prepared in phosphate buffered saline (PBS) at a concentration of 5 mg/ml. 400 µl MTT is added to each well and incubated at 37 °C for 4 hrs. At the end of the incubation, the medium is discarded and replaced by 4 ml dimethylsulfoxide (DMSO). The absorbance (OD: Optical Density) of the samples is measured on a microplate reader (Hiperion MPR4+). The cell viabilities are expressed as $OD_{sample}OD_{negative\ control}^{-1}* 100\%$, where OD_{sample} and $OD_{negative}$ control are the absorbance of the sample and the control, respectively. Cell morphology is observed by using SEM. For the cell observation, cells on samples are fixed by 2.5% glutaraldehyde solution and rinsed three times with phosphate buffer solution (PBS, pH 7.4). The samples are then dehydrated in 30, 50, 70, 90, 95 and 100 vol. % alcohol solutions, successively. Statistical analysis is conducted to evaluate the difference in cell viability using student's t-test. The significant differences between the means of two samples are compared. For this purpose t value is calculated based on the $t = (x_1 - x_2) / S_d$, where x_1, and x_2 are the mean of values and S_d is the variance of the difference between the means. The statistical significance is defined as 0.05. The data are expressed in mean ± SD.

3. RESULTS AND DISCUSSION

3.1 Surface Characterization

Fig. 2a shows the XRD patterns of AZ91 and ASD-coated samples. In the AZ91 substrate pattern, the Mg peaks are display while for the ASD coating, Mg, MgO and Mg_2SiO_4 peaks are observed. MgO is formed by dissolving Mg^{2+} from the substrate and the O^{2-} from the electrolyte by the reaction $Mg^{2+} + O^{2-} \rightarrow$ MgO. At high temperature, both SiO_2 and MgO are present in the fused state [27]. However, during the sparks and by the cooling effect of the electrolyte, SiO_2 and MgO will react to form Mg_2SiO_4 according to reaction $SiO_2 + 2MgO \rightarrow Mg_2SiO_4$. The mechanism of apatite formation is well-known in Mg_2SiO_4 (forsterite) containing coatings, and it has been reported by other investigators [28] that decomposition of forsterite can form negative silanol groups (Si–OH–), and in this way it can absorb Ca^{2+} and PO_4^{3-} ions respectively on its surface. Fig. 2b shows SEM images from the cross–sectional view along with the line scan EDS analysis from the ASD coating until the AZ91 substrate. As can be seen in Fig. 2b, the thickness of ASD coating is about 100 μm. The line–scan EDS analysis confirms that the coating mainly consists of Mg and O elements. The intensity of O decreases progressively from coating to substrate of ASD, while that of Mg shows an opposite trend. The SEM images from the top view of ASD coating, show the volcano–like structure on the surface with some porosities (Fig. 2c, d). This structure is formed by the gas bubbles during the anodic spark deposition. The ASD coating is composed of one outer porous layer and one inner compact barrier layer. The inner layer in contact with the Mg substrate is compact and uniform. This inner layer can be a simple partial barrier to diffusion of corrosive solution to the substrate. But, the outer layer is coarse with many micro-holes and micro-cracks. The gas bubbles in the coating growth process produced porosity on the outer layer of ASD coating, and the micro-cracks are formed because of the thermal stress due to the rapid solidification of the molten oxide in the cooling electrolyte. Thus, the inner compact layer can insulate the substrate from the corrosive electrolyte ions to improve the corrosion resistance of ASD coating. However, the outer layer of ASD coating would absorb more corrosive electrolyte and decrease the corrosion resistance of the ASD coating on the Mg alloy substrate. Fig. 2 also shows the laser scanning electron microscopy images with two dimension (2-D) (e), three dimension (3-D) (f), and profilometry analysis (g) from the surface of ASD coated samples. According to laser scanning microscope images, ASD coating has a rough and porous morphology. Imaging the various parts of the sample revealed that the islands with different heights formed on the surface of ASD coating (red and Blue Island which are observed on the Fig 2e, f). Overall, roughness of the red and blue parts on the three dimensional images is calculated between 5 to 20 μm, according to the profilometer of VK analyzer (Fig. 2g).
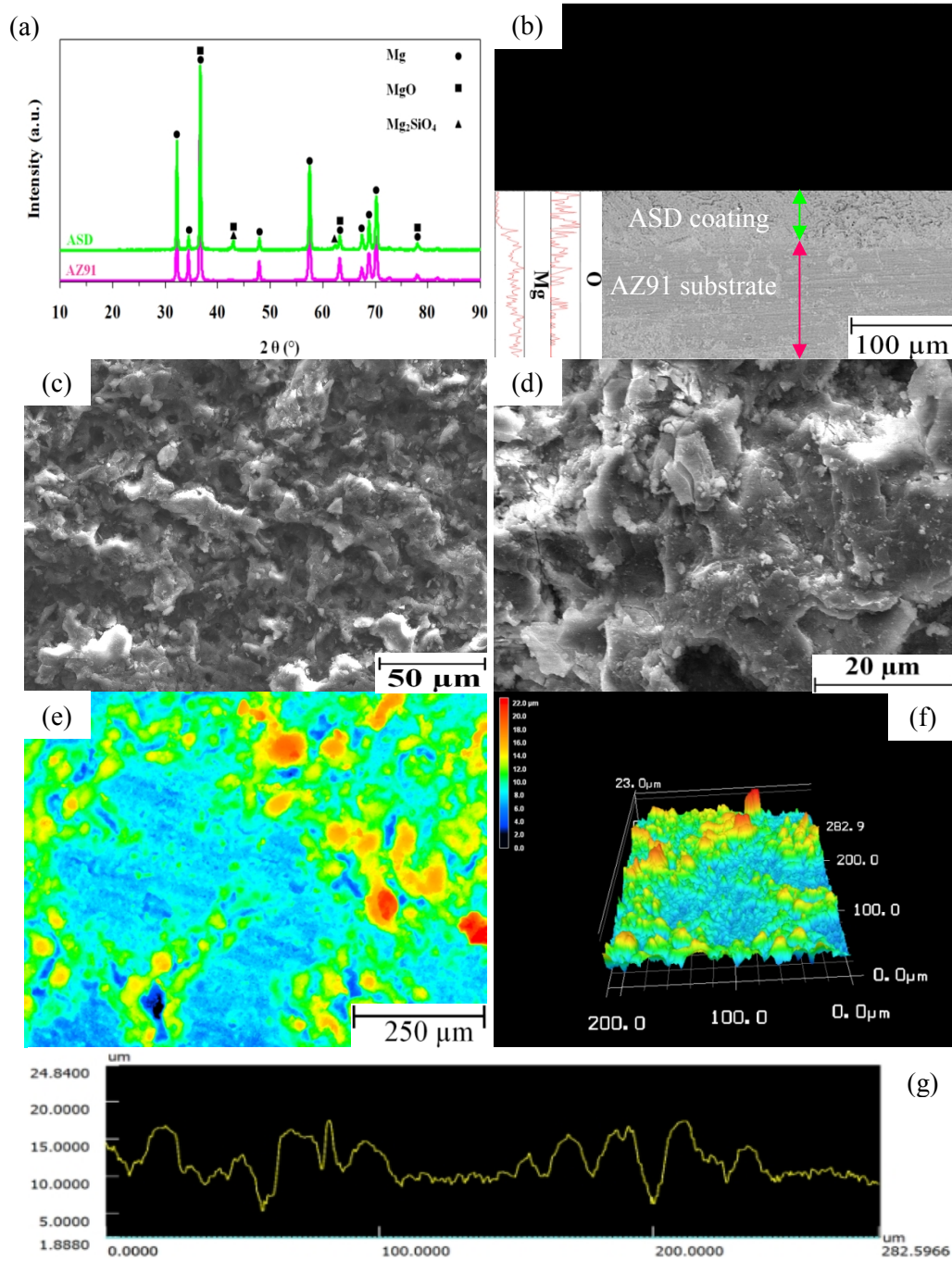
Fig. 2. XRD patterns of AZ91 and ASD-coated samples (a), SEM images from the cross–sectional view along with the line scan EDS analysis from the ASD coating until the AZ91 substrate (b), SEM images from the top view of ASD coating in different magnifications (c,d), laser scanning electron microscopy images including two dimensional (2-D) (e), three dimensional (3-D) (f), and profilometry analysis (g) from the surface of ASD coated samples

3.2 Corrosion Testing

Fig. 3 shows the EIS spectra containing (a) Bode and (b) Phase plots for the AZ91 and ASD-coated samples in the SBF. The electrochemical corrosion parameters of the AZ91 and ASD-coated samples are summarized in Table 1. In order to interpret the plots, an equivalent circuit is proposed using ZSimpDemo 3.30d software. The corresponding fitted data are presented in Fig. 3c. The EIS fitted results of the above samples are summarized in Table 1.

In (a) Bode and (b) Phase plots (see Fig. 3), three loops including two capacitive and one inductive are seen for all samples, similar to previous reports on Mg [29]. These loops are a capacitive loop in the high frequency region, a capacitive loop in the middle frequency region, and a pseudo inductive loop in the low frequency region. The capacitive loop in the high frequency range may be related to the charge transfer reaction and the diameter of the loop is proportional to the value of the transfer resistance R_t. The larger the value of R_t, the better is the corrosion protective property of ceramic coating. The capacitive loop in the middle frequency is related to mass transportation in the solid phase and the pseudo inductive loop is because of the absorption processes [17]. The Faraday charge transfer resistance, R_t, is related to the electrochemical reaction in the same region. From R_t value, the exchange–current density (j_0) could be calculated using the following expression (Eq. 1) [30]:

$$J_0 = RT/nFR_t \tag{1}$$

where n, and F are the number of transferred charges and Faraday constant, respectively. Apparently, j_0 is in inverse proportion to R_t, in other words, the higher R_t is, the lower the corrosion rate would be [29].

Accordingly, charge transfer resistance is utilized to estimate the corrosion resistance of the samples. This is because an increase in j_0 should correspond to an increase in the corrosion rate. It can be deduced from EIS spectra that R_t of AZ91 samples increase from 137.6 Ω cm^2 to 439.7 Ω cm^2 for ASD-coated samples, suggesting that the ASD coating is more corrosion resistant than AZ91.

R_p is called the polarization resistance. The ASD-coated sample shows a larger R_p implying a good corrosion resistance on the surface. The EIS data according to Table 1 reveal that the ranking of R_p is as follows: ASD (957.2 ohm) > AZ91 (305.5 ohm).

In Fig. 3 and Table 1, R_s is the solution resistance between the reference electrode and working electrodes. Its value depends on the conductivity of test medium as well as geometry of the cell [17].

C_f is one of the constant phase element (CPE) components and represents the capacitance of the intact coating on the surface. A larger value of C_f indicates that the dielectric constant of surface coating increases due to the electrolyte penetration caused by chemical dissolution. Thus, as in Table 1, the ASD coated sample has more protective propensity than the uncoated ones.

C_{dl}, another CPE component, denotes the capacitance of the interface electric double layer in the vulnerable regions exposed to the electrolyte penetration. The variation of C_{dl} can be attributed to the deterioration of surface coating resulting in a larger area fraction of the

vulnerable regions. The capacitance of double layer, C_{dl}, that shows the typical metal/solution system, varies from 10 to 100 µF [17]. In Table 1, the values of C_{dl} in current experiments are all in this range.
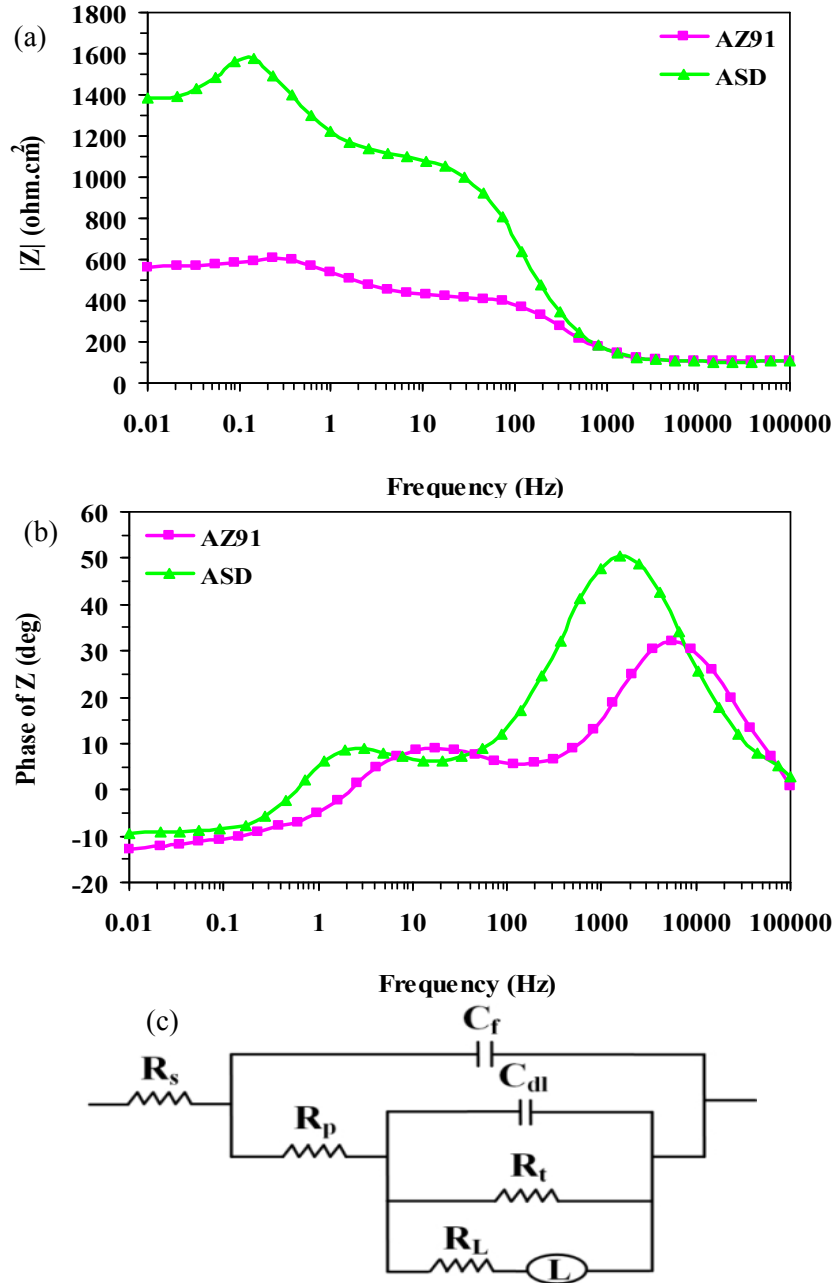

Fig. 3. EIS spectra containing Bode (a) and Phase (b) plots for the AZ91 and ASD-coated samples in the SBF and equivalent circuit in order to model the sample/solution system (c)

Here, larger values of R_p and R_t also correspond to smaller C_f and C_{dl}, respectively. In addition, L expresses the inductance and R_L is the low frequency loop resistance. Also, m and n are indices of the dispersion effects of C_f and C_{dl}, respectively which represent their deviations from the ideal capacitance due to the inhomogeneity and roughness of electrode on the micro scale [22]. The values of m and n are always 0 < m and n < 1. The values of m and n in the current experiments are all in this range.

The corrosion test results of this study indicate that the corrosion resistance of AZ91 is significantly increased by applying the surface coating that is prepared via the ASD method.

Table 1. The electrochemical corrosion parameters of the AZ91 and ASD-coated samples

Samples	I_{corr} (nA/cm^2)	E_{corr} (V_{SCE})	R_s (Ω cm^2)	C_f (10^{-6}Fcm^{-2})	R_p (Ω cm^2)	C_{dl} (10^{-6}Fcm^{-2})	R_t (Ω cm^2)
AZ91	63100	-1.6	105.5	4.2	305.5	68	137.6
ASD-coated	53700	-1.56	111.3	3.8	957.2	53	439.7

Fig. 4 shows the SEM morphology of (a) AZ91 and (b,c) ASD samples after 672 hrs immersion in the SBF. Some areas of the AZ91 and ASD surfaces are corroded with large and deep cracks while some white particles are found precipitated on these surfaces.

The cracks of AZ91 sample are more than those of the ASD-coated samples. In contrast, the density of precipitated white particles of ASD-coated sample is more than AZ91 sample.

In Fig. 4d the FTIR spectrum shows precipitated white particles on the surface of ASD-coated samples after 672 hrs immersion in the SBF. The layer contained CO_3^{2-} and PO_4^{3-} groups. This kind of products and its structure may refer to the bioactive minerals that could be suitable for bone implant materials. Due to the presence of intermetallic phases such as $Mg_{17}Al_{12}$ along with the grain boundaries, the microgalvanic corrosion occurred between the intermetallic phase and untreated AZ91 matrix [31], which resulted in the intergranular corrosion in AZ91 sample. For ASD-coated sample, the corrosive media diffused through the substrate and Hydrogen bubbles released from the substrate [32], which led to the formation of cracks in ASD coating layer.

The physical and chemical alterations of a material in physiological medium, which result in the deterioration and dissolution of material, is called biodegradation. The chemical changes lead to the dissolution and physical alterations cause falling off the particles from the substrate. Regarding the magnesium alloy, releasing the hydrogen bubbles from the magnesium implant may lead to particles of ASD coating falling off from the surface. The released particles can be dissolved afterward due to the high surface area of particles.

Fig. 5a shows the weight loss of AZ91 and ASD-coated samples in the SBF solution versus immersion time. The weight loss of the ASD-coated samples is less than that of the AZ91 samples. After 672h, the weight loss of AZ91 and ASD-coated samples were about 31.8 and 19.9%, respectively.

Fig. 5b shows the degradation rate of AZ91 and ASD-coated samples in terms of weight loss. The degradation rate of all groups dropped sharply between 72 and 168 hrs, but it slowly decreases after 168 hrs immersion until the end of the experiment. This could be attributed to the formation and precipitation of degradation products, which protects the

substrate in longer times. The degradation rate of AZ91 sample is significantly higher than that of the ASD-coated sample for all the selected immersion times.

According to Fig. 5c, the release of Mg ion on the first 72 hrs is the highest, decreased between until the 168 hrs and reached a stable state up to the end of the immersion. The highest concentration is found for the uncoated AZ91 sample, indicating the highest degradation rate among the tested samples. All the ASD-coated samples have significantly lower release of Mg ions during the immersion test.

When the samples are immersed in the SBF, the pH of the SBF solution is monitored, and the results are shown in Fig. 5d. The same pattern is observed in the pH plot with immersion time for all samples. The pH value increases rapidly from 0 to 72 hrs immersion, then decreases slowly from 72 to 168 hrs and reached a stable value afterward. The reactions between magnesium and corrosive medium can be summarized as below:

$$Mg \rightarrow Mg^{2+} + 2e^- \tag{2}$$

$$2H_2O + 2e^- \rightarrow H_2 + 2OH^- \tag{3}$$

$$Mg + 2H_2O \rightarrow Mg^{2+} + H_2 + 2OH^- \tag{4}$$

$$Mg^{2+} + 2OH^- \rightarrow Mg(OH)_2 \tag{5}$$

$$Mg(OH)_2 + 2Cl^- \rightarrow MgCl_2 + 2OH^- \tag{6}$$

During the 72 to 168 hrs immersion, the pH value of all solutions declined, which can be attributed to the formation of corrosion products including magnesium hydroxide (reaction 5) and apatite on the surface. These products consume OH^- group from the solution leading to a decrease in pH value [32,33]. It is worth noting that at the initial stages of immersion in a Cl^- containing solution, the corrosion rate of magnesium is high due to the lack of deposition of thick passive layer leading to the dissolution of magnesium hydroxide and increasing the pH value (reaction 6). However, in prolonged times, deposition of a thick magnesium hydroxide layer is dominated, which leads to a decrease in the pH value (reaction 5).The slow increase in the pH value of the solution for the samples with the ASD coating during first 72 hrs indicates a relatively slow chemical dissolution and an improvement in the degradation resistance of the ASD coating.

Fig. 6 shows the surface morphology of AZ91 (a) and ASD-coated (b) samples immersed for 672 hrs in the SBF after removal of the degradation product at different magnifications. The AZ91 sample shows obvious degradation and the defect expanded from the edge to the centre while the surface is full of web–like cracks and deep pits, resulting in marked weight loss of AZ91 substrate. This implies the uncoated AZ91 alloy suffered from localized severe degradation attack as shown in Fig. 6a. In contrast, it is observed that the ASD-coated samples are subjected to a milder and more uniform corrosion attack than the uncoated AZ91 sample as shown in Fig. 6b. After soaking in the SBF for 672 hrs, the coated sample kept its shape integrity with the presence of few pits on the surface, and there exist only slightly attacked degradation spots on the as–cleaned ASD-coated samples. The depth of the degradation pits is shallower than that of the substrate. In other words, the residual area of the ASD-coated sample is larger than that of the substrate. This is mainly because of the diffusion of corrosive media into the Mg substrate through the micro-pores existing in the ASD coating, resulting in the degradation attack. However, this decrease in degradation

reaction reveals that the ASD coating on Mg alloy could in fact guard the substrate from degradation attacks during the immersion tests by acting as an useful passive layer in opposition to electrolyte entrance into the underlying Mg substrate.
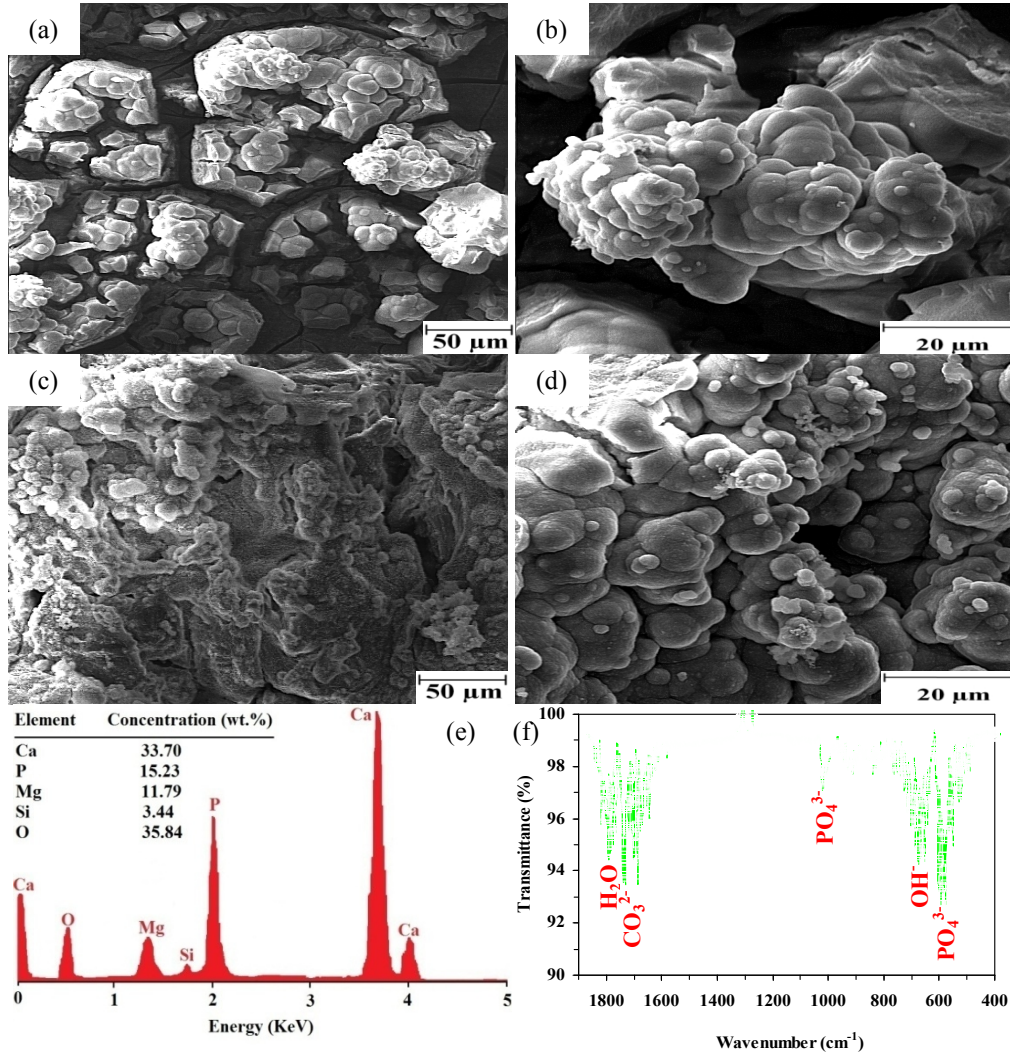

Fig. 4. SEM morphology of AZ91 (a), and ASD (b,c) samples after 672 hrs immersion in the SBF and FTIR spectrum of the precipitated white particles on the surface of ASD-coated samples after 672 hrs immersion in the SBF (d)
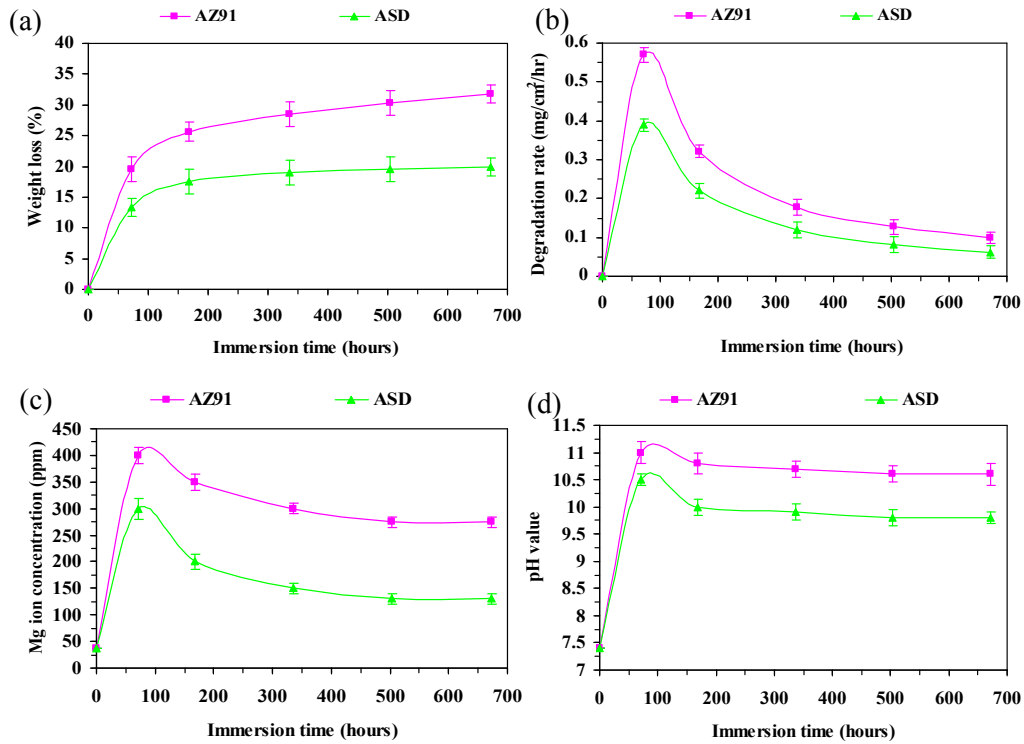
Fig. 5. Weight loss (a), degradation rate (b), Mg ion concentration (c), and pH value (d) of AZ91 and ASD-coated samples immersed in the SBF versus immersion time
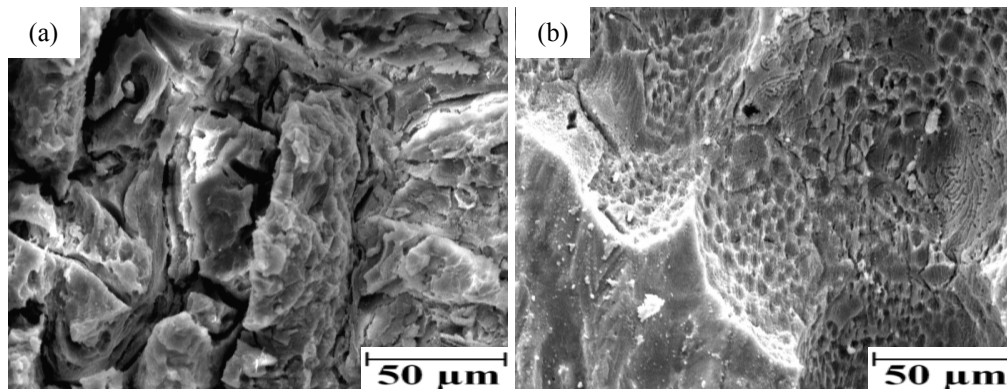

Fig. 6. Surface morphology of AZ91 (a, c) and ASD-coated (b, d) samples immersed for 672 hrs in the SBF after removal of the degradation products in different magnifications

3.3 Mechanical Testing

In vitro mechanical stability studies are carried out by compression test on the AZ91 and ASD-coated samples before and after immersion in the SBF for 4 weeks. Stress–strain curves for the AZ91 and ASD-coated samples are shown in Fig. 7, and their compressive

properties are summarized in Table 2. Since the ASD coating did not change the initial mechanical properties of the AZ91 sample, the stress–strain curves of AZ91 and ASD-coated samples are found to be similar before immersion (i.e. time point 0).

The compressive yield strength of the ASD-costed sample after 1 month immersion in the SBF is more than that of the AZ91 sample. The compressive strength of ASD-coated sample after 4 weeks immersion decreases from 160 MPa to 90 MPa. However, that of the AZ91 sample drops to 75 MPa after 4 weeks immersion. The compressive strengths of ASD-coated samples remained 15 MPa higher than the uncoated AZ91 samples after 4 weeks of immersion. This is largely due to the slower corrosion rate which indicates that the ASD coating delayed the loss of mechanical property of the substrate. Generally, the compressive strength of human bones is 100–230 MPa in cortical bone and 2–12 MPa in cancellous bone [34]. The results show that the compressive strength of ASD-coated samples after 4 weeks is only slightly below the strength of human cortical bone.
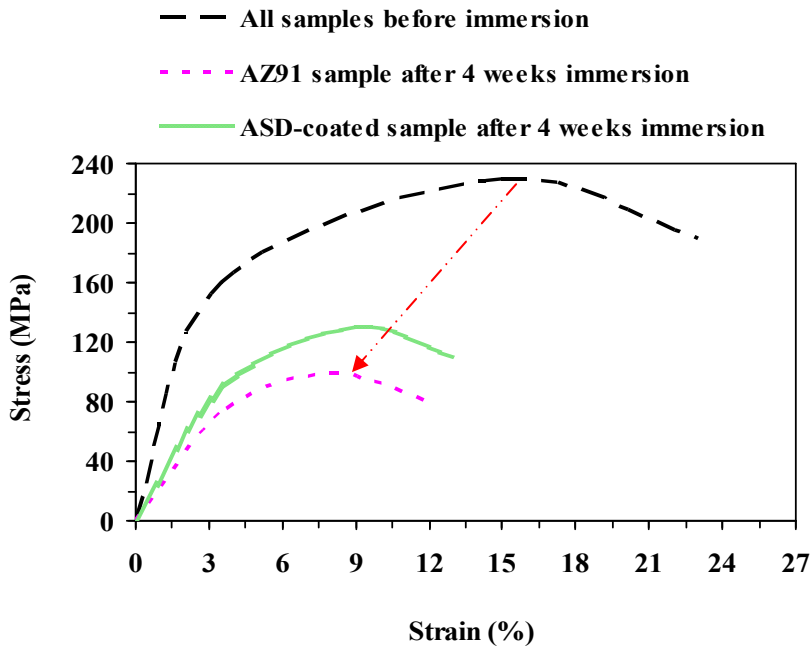

Fig. 7. Stress–strain curves for the AZ91 and ASD-coated samples before and after immersion

Table 2. Compressive properties of the AZ91 and ASD-coated samples before and after 4 weeks immersion in the SBF

Samples	Compressive yield strength, (MPa)	Compressive strength, (MPa)
All samples before immersion	160	230
AZ91 sample after 4 weeks immersion	75	100
ASD-coated sample after 4 weeks immersion	90	130

3.4 Biocompatibility Studies

Fig. 8a presents the relative cell viability (% of control) of L–929 cells after 2, 5, and 7 days of incubation on the AZ91 and ASD-coated samples. The cell viability is found to increase with culture time, indicating that the cells could attach and proliferate on the surface of samples. For the uncoated AZ91 samples, there is no significant increase in the cell viability during the whole incubation period. The cell viability on the uncoated AZ91 samples changed from 50 % at 2 days incubation to 58 % at 7 days incubation, indicating that the uncoated AZ91 samples do not encourage the cell growth well enough. In comparison with the AZ91 samples, the cell viability on the ASD-coated samples exhibits a statistically significant increase at all time intervals. ASD-coated sample's cell viability increase from 70 to 85 % for 2 and 7 days incubation periods respectively. This result indicates that the ASD-coated samples significantly improve cytocompatibility compared to the uncoated ones.

Fig. 8 also presents the SEM images from the surface of AZ91 (b), and ASD-coated (c,d) samples after 7 days cell culture which indicate the different cell response to the different surfaces. The localized corrosion and micro cracks are also detected on the surface of AZ91 samples (Fig. 8b). For the ASD-coated samples, the cells are confluent and the area in use by the cells on the surface increase significantly during the cell culture experiment (Fig. 8c). The cells spread and connected together with spherical morphology on the cell surfaces, which implies mineralization. The improve cell spreading is observed on the ASD-coated samples. Moreover, in comparison with the AZ91 sample, more cells spread and attached to the surface of the ASD-coated samples. The inset in Fig. 8 is selected from one of the cells showing the filopedia around the spherical morphology of cells. Regarding the spherical morphologies of cells, the geometry of fibroblast cells can be varied depending on the cell density and substrate morphology. In addition, change in cell configuration is notably affected by arrangement of actin filaments. The difference in cell morphology of fibroblasts grown in various substrates may be related to differences in the amount of actin filamentous in the cell. Spherical morphology can be observed in fibroblast cells with higher amount of actin filamentous. Difference in the morphology of cells may also be related to the variations in the extra cellular matrix (ECM) properties, since the porous surfaces can imitate the gaps that permeate the damaged ECM of the wound site, which may lead to adoption of a round morphology of cells [35,36].

During Mg dissolution, the amount of Mg ions increases in the media and substrate corrosion produces a product layer which gradually peels out from the surface [37]. These occurrences along with release of hydrogen bubbles from the Mg alloy cause complexity in cell attachment process. The better cell response and biocompatibility of the ASD-coated samples may be attributed to samples enhanced corrosion resistance. Therefore, more cells can adhered on the surface of coated samples which then spread and proliferate to form confluent [38].
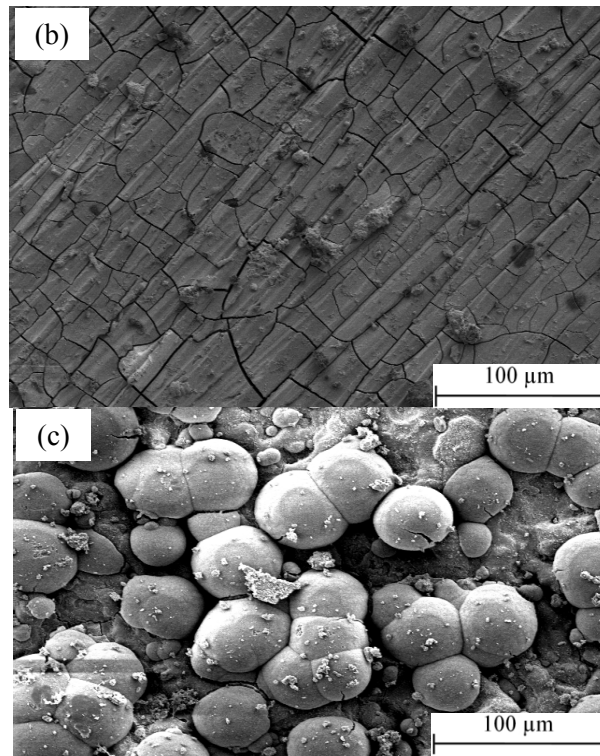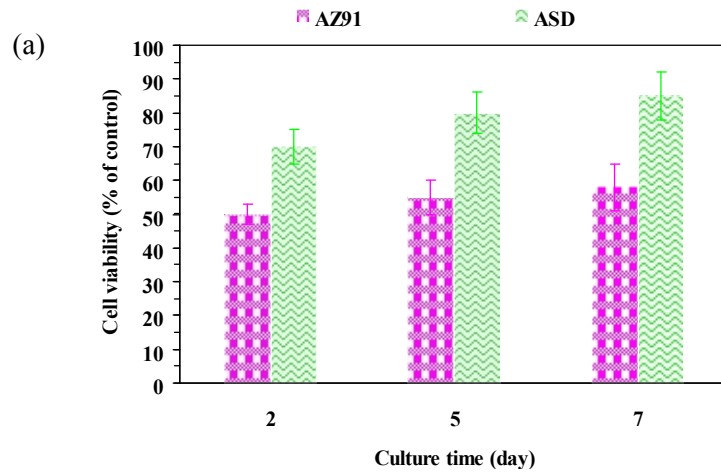
Fig. 8. Relative cell viability (% of control) of L–929 cells after 2, 5, and 7 days of incubation on the AZ91 and ASD-coated samples and the SEM images from the surface of AZ91 (b), and ASD-coated (c) samples after 7 days cell culture

4. CONCLUSION

This study has shown that the corrosion resistance, *in vitro* bioactivity, mechanical integrity and cytocompatibility of biodegradable Mg alloy can be improved by ASD coating method. The results indicate that the rapid degradation of Mg occurring at the interface between the

AZ91 substrate and the corrosive media adversely affects the cell growth. Proper reduction of the degradation rate by ASD coating not only makes a stable surface for the cell adhesion and growth, but also declines the release of degradation products to decreases the cytotoxicity. This results in enhanced cytocompatibility. However, multiple cell lines are needed to prove the biocompatibility of ASD coated magnesium alloy, which is our future research trend.

ETHICAL APPROVAL

All authors hereby declare that "Principles of laboratory animal care" are followed, as well as specific national laws where applicable. All experiments have been examined and approved by the appropriate ethics committee.

COMPETING INTERESTS

Authors have declared that no competing interests exist.

REFERENCES

1. Staiger MP, Pietak AM, Huadmai J, Dias G. Magnesium and its alloys as orthopedic biomaterials: a review. Biomaterials 2006;27:1728-34.
2. Rouhani P, Salahinejad E, Kaul R, Vashaee D, Tayebi L. Nanostructured zirconium titanate fibers prepared by particulate sol–gel and cellulose templating techniques. Journal of Alloys and Compounds 2013;568:102-5.
3. Shahini A, Yazdimamaghani M, Walker KJ, Eastman MA, Hatami-Marbini H, Smith BJ, et al. 3D conductive nanocomposite scaffold for bone tissue engineering. International journal of nanomedicine. 2014;9:167.
4. Kirkland N, Lespagnol J, Birbilis N, Staiger M. A survey of bio-corrosion rates of magnesium alloys. Corrosion Science. 2010;52:287-91.
5. Witte F. The history of biodegradable magnesium implants: A review. Acta Biomaterialia. 2010;6:1680-92.
6. Zheng Y, Gu X, Witte F. Biodegradable metals. Materials Science and Engineering: R: Reports. 2014;77:1-34.
7. Witte F, Fischer J, Nellesen J, Crostack H-A, Kaese V, Pisch A, et al. In vitro and in vivo corrosion measurements of magnesium alloys. Biomaterials. 2006;27:1013-8.
8. Kirkland N, Birbilis N, Staiger M. Assessing the corrosion of biodegradable magnesium implants: A critical review of current methodologies and their limitations. Acta biomaterialia. 2012;8:925-36.
9. Xu L, Pan F, Yu G, Yang L, Zhang E, Yang K. In vitro and in vivo evaluation of the surface bioactivity of a calcium phosphate coated magnesium alloy. Biomaterials. 2009;30:1512-23.
10. Hornberger H, Virtanen S, Boccaccini A. Biomedical coatings on magnesium alloys–A review. Acta biomaterialia. 2012;8:2442-55.
11. Salahinejad E, Hadianfard M, Macdonald D, Mozafari M, Vashaee D, Tayebi L. A new double-layer sol–gel coating to improve the corrosion resistance of medical-grade stainless steel in a simulated body fluid. Materials Letters; 2013.
12. Li J, Han P, Ji W, Song Y, Zhang S, Chen Y, et al. The in vitro indirect cytotoxicity test and in vivo interface bioactivity evaluation of biodegradable FHA coated Mg–Zn alloys. Materials Science and Engineering: B. 2011;176:1785-8.

13. Razavi M, Fathi M, Savabi O, Hashemi Beni B, Vashaee D, Tayebi L. Nanostructured merwinite bioceramic coating on Mg alloy deposited by electrophoretic deposition. Ceramics International. 2014;40:9473-9484.

14. Razavi M, Fathi M, Savabi O, Mohammad Razavi S, Hashemi Beni B, Vashaee D, et al. Controlling the degradation rate of bioactive magnesium implants by electrophoretic deposition of akermanite coating. Ceramics International. 2013;40:3865-3872.

15. Razavi M, Fathi MH, Savabi O, Vashaee D, Tayebi L. Biodegradation, bioactivity and in vivo biocompatibility analysis of plasma electrolytic oxidized (PEO) biodegradable Mg implants. Physical Science International Journal. 2014;4:708-22.

16. Blawert C, Dietzel W, Ghali E, Song G. Anodizing treatments for magnesium alloys and their effect on corrosion resistance in various environments. Advanced Engineering Materials. 2006;8:511-33.

17. Zhang Y, Yan C, Wang F, Li W. Electrochemical behavior of anodized Mg alloy AZ91D in chloride containing aqueous solution. Corrosion Science. 2005;47:2816-31.

18. Qian J-g, Wang C, Li D, Guo B-l, Song G-l. Formation mechanism of pulse current anodized film on AZ91D Mg alloy. Transactions of Nonferrous Metals Society of China 2008;18:19-23.

19. Shang W, Chen B, Shi X, Chen Y, Xiao X. Electrochemical corrosion behavior of composite MAO/sol–gel coatings on magnesium alloy AZ91D using combined micro-arc oxidation and sol–gel technique. Journal of Alloys and Compounds. 2009;474:541-5.

20. Wang Y, Guo J, Shao Z, Zhuang J, Jin M, Wu C, et al. A metasilicate-based ceramic coating formed on magnesium alloy by microarc oxidation and its corrosion in simulated body fluid. Surface and Coatings Technology. 2013;219:8-14.

21. Chen F, Zhou H, Yao B, Qin Z, Zhang Q. Corrosion resistance property of the ceramic coating obtained through microarc oxidation on the AZ31 magnesium alloy surfaces. Surface and Coatings Technology. 2007;201:4905-8.

22. Xu J, Liu F, Wang F, Yu D, Zhao L. The corrosion resistance behavior of Al_2O_3 coating prepared on NiTi alloy by micro-arc oxidation. Journal of Alloys and Compounds 2009;472:276-80.

23. Kokubo T, Takadama H. How useful is SBF in predicting in vivo bone bioactivity? Biomaterials. 2006;27:2907-15.

24. ASTM-G31-72:. standard practice for laboratory immersion corrosion testing of metals, Annual book of ASTM standards. American Society for Testing and Materials, Philadelphia, PA, USA; 2004.

25. Chiu K, Wong M, Cheng F, Man H. Characterization and corrosion studies of fluoride conversion coating on degradable Mg implants. Surface and Coatings Technology. 2007;202:590-8.

26. E9 A. Standard Test Method of Compression Testing of Metallic Materials at Room Temperature. Annual Book of ASTM Standards; 2000.

27. Li Z, Gu X, Lou S, Zheng Y. The development of binary Mg–Ca alloys for use as biodegradable materials within bone. Biomaterials. 2008;29:1329-44.

28. Kharaziha M, Fathi M. Synthesis and characterization of bioactive forsterite nanopowder. Ceramics International. 2009;35:2449-54.

29. Song G, Atrens A, Wu X, Zhang B. Corrosion behaviour of AZ21, AZ501 and AZ91 in sodium chloride. Corrosion Science. 1998;40:1769-91.

30. Udhayan R, Bhatt DP. On the corrosion behaviour of magnesium and its alloys using electrochemical techniques. Journal of power sources. 1996;63:103-7.

31. Song G, Bowles AL, StJohn DH. Corrosion resistance of aged die cast magnesium alloy AZ91D. Materials Science and Engineering: A. 2004;366:74-86.

32. Wong HM, Yeung KW, Lam KO, Tam V, Chu PK, Luk KD, et al. A biodegradable polymer-based coating to control the performance of magnesium alloy orthopaedic implants. Biomaterials. 2010;31:2084-96.

33. Kim H-M. Ceramic bioactivity and related biomimetic strategy. Current opinion in solid state and materials science. 2003;7:289-99.

34. Razavi M, Fathi M, Meratian M. Microstructure, mechanical properties and bio-corrosion evaluation of biodegradable AZ91-FA nanocomposites for biomedical applications. Materials Science and Engineering: A. 2010;527:6938-44.

35. Glasser H, Fuhr G. Cultivation of cells under strong ac-electric field—differentiation between heating and trans-membrane potential effects. Bioelectrochemistry and bioenergetics. 1998;47:301-10.

36. Grace LHY, Wah TY. Effect of collagen gel structure on fibroblast phenotype; 2012.

37. Song G, Atrens A, John DS, Wu X, Nairn J. The anodic dissolution of magnesium in chloride and sulphate solutions. Corrosion Science. 1997;39:1981-2004.

38. Ilich JZ, Kerstetter JE. Nutrition in bone health revisited: a story beyond calcium. Journal of the American College of Nutrition. 2000;19:715-37.